HHS Public Access

Author manuscript

Photodiagnosis Photodyn Ther. Author manuscript; available in PMC 2021 July 23.

Published in final edited form as:

Photodiagnosis Photodyn Ther. 2020 June ; 30: 101704. doi:10.1016/j.pdpdt.2020.101704.

Multispectral autofluorescence dermoscope for skin lesion assessment

Renan Arnon Romano[#a], **Ramon Gabriel Teixeira Rosa**[#a], **Ana Gabriela Salvio**[b], **Javier A. Jo**[c], **Cristina Kurachi**[a]

[a]São Carlos Institute of Physics, University of São Paulo, P.O. Box 369, 13560-970, São Carlos, SP, Brazil

[b]Skin Department of Amaral Carvalho Hospital, Jaú, SP, Brazil

[c]School of Electrical and Computer Engineering, University of Oklahoma, Norman, OK, USA

[#] These authors contributed equally to this work.

Abstract

Basal cell carcinoma (BCC) is the most common type of skin cancer. Diagnosis and edge assessment of BCC lesions are based on clinical and dermoscopy evaluation, which are strongly dependent on the expertise and training of the physician. There is a high rate of underdiagnosis because BCC is frequently confused with certain common benign lesions and is often indistinguishable from the surrounding healthy tissue. In the present study, a multispectral fluorescence lifetime imaging (FLIm) dermoscopy system, designed for imaging and analyzing the autofluorescence emission of skin tissue, was used to image thirty-eight patients with diagnosed nodular BCC (nBCC) lesions, using clinically acceptable levels of excitation light exposure. With this system, skin autofluorescence was imaged simultaneously using three emission bands: 390±20 nm, 452±22 nm, and >496 nm, preferentially targeting collagen, NADH, and FAD autofluorescence, respectively. Statistical classifiers based on FLIm features developed to discriminate BCC from healthy tissue showed promising performance (ROC area-under-the-curve of 0.82). This study demonstrates the feasibility of clinically performing multispectral endogenous FLIm dermoscopy providing baseline results indicating the potential of this technology as an image-guided tool to improve the delineation of nBCC during surgical lesion resection.

Keywords

Label-free fluorescence; Fluorescence lifetime imaging; In vivo; Skin cancer; BCC

1. Introduction

Basal cell carcinoma (BCC) is the most frequent skin cancer in fair skinned people worldwide. Global incidence rates vary from 1 to 1000/100000 person-years, with an average of 47/100000 person-years. The average incidence rates for Brazil and England are around 79/100000 and 76/100000 person-years [1–3]. Although BCC has a low mortality rate, non-melanoma skin cancer has high morbidity as a result of the high rate of recurrence and formation of multiple lesions [4,5]. BCC also constitutes a diagnostic challenge, since it

may be clinically similar to benign lesions, especially during the early stages of the disease [5–7]. Another major problem in the clinical management of BCC is the difficulty in precisely delineating the BCC lesion margins during surgical resection [5]. After excision, recurrence rates range from 4% to 66 %, depending on the skill of the dermatologist and the BCC subtype [4–6,8].

Clinical detection of skin cancer is based on subjective cues including lesion roughness, color, and shape, as well as other characteristics such as progression time and presence of ulceration. Therefore, detection is highly dependent on physician training and expertise. This creates a challenge for early diagnosis and border detection of small lesions of skin cancer, particularly in populations with limited access to properly trained dermatologists and/or adequate clinical infrastructure [6,7,9]. Common diagnosis methods, such as cytology or histopathology, are invasive and require laboratory processing, thus limiting treatment monitoring and comprehensive screening of large lesions [6].

Epithelial tissue autofluorescence is mainly attributed to three endogenous fluorophores: collagen, flavin adenine dinucleotide (FAD), and reduced nicotinamide adenine dinucleotide (NADH). Epithelial cancer cells use different metabolic pathways, compared to normal epithelial cells [10], resulting in subtle but measurable changes in their attributed autofluorescence [11,12]. Morphological changes in the epithelial tissue structure, associated with pathological tissue transformation, can also result in changes in the collagen-attributed tissue autofluorescence emission [13]. Therefore, autofluorescence spectroscopy and imaging could potentially enable nondestructive detection of epithelial cancer [14–16].

A number of studies have been carried out to distinguish between non-melanoma skin cancers and healthy tissue, based on tissue autofluorescence characterization [13– 19]. Steady-state fluorescence emissions of tryptophan, collagen, elastin, NADH, and FAD have been reported to distinguish between BCC and a healthy surrounding region [14,18]. In vivo human studies have found that collagen-related fluorescence intensity decreases in the BCC region, compared to the normal tissue [14]. Furthermore, studies have reported reduced autofluorescence intensities at the spectral emission peaks of NADH and FAD for BCC lesions, compared to healthy tissue [15,18]. Despite observing differences in the autofluorescence intensity profiles, Galletly et al. reported low values for accuracy when distinguishing between healthy and BCC tissues [15].

Skin autofluorescence lifetimes have been investigated by FLIM (fluorescence lifetime imaging microscopy) in animal models [19] as well as in ex vivo [15,17,20–22] human biopsies. In a study using an orthotopic mouse model of human cutaneous squamous cell carcinoma (SCC), the lifetime of the FAD-attributed tissue autofluorescence was found to be shorter in SCC than in healthy tissue; however, it was not possible to achieve highly accurate lesion classification, based on this lifetime [19]. In a study with human ex vivo skin lesions, the lifetimes of tissue autofluorescence induced with 355 nm and 435 nm excitations and measured across the visible spectrum were found to be significantly different among BCC, SCC, and seborrheic keratosis; however, healthy tissue was not characterized, and the small sample size did not allow quantification of classification performance [17]. In another study with human ex vivo skin lesions, FLIM images of 25 BCC lesions were acquired using 355

nm excitation and broadband visible emission spectrum collection [15]. Significant reductions in average fluorescence lifetimes were observed between areas of BCC and areas of surrounding uninvolved skin. Moreover, the distinction of BCC areas from surrounding uninvolved skin tissue, based on autofluorescence lifetimes, was significantly more accurate than when using autofluorescence intensities (ROC-AUC: ~0.9 for lifetimes vs. ~0.6 for intensities).

Using a time domain fluorescence lifetime spectroscopy system to investigate cutaneous melanoma in an animal model, a study showed 98 % accuracy to distinguish between healthy skin and melanoma [23]. Same system was used in a study with human in vivo skin lesions, the lifetimes of tissue autofluorescence induced with 378 nm excitation and measured at the NADH and FAD spectral emission peaks were found to be significantly shorter for BCC lesions, compared to normal tissue; however, the small sample size did not allow quantification of classification performance [16].

This study reports on the use of a time-domain multispectral fluorescence lifetime imaging (FLIm) dermoscope, demonstrating its ability to perform clinical multispectral fluorescence lifetime dermoscopy of nodular BCC (nBCC) lesions. Preliminary results based on FLIm images acquired from 38 patients indicated the potential of endogenous FLIm endoscopy as an image-guided tool to improve the delineation of nBCC lesions during surgical lesion resection.

2. Methods

2.1. FLIm system for clinical imaging of skin lesions

The FLIm imaging system used in this study was a modified version of a previous design [24], adapted for clinical imaging of skin lesions. A schematic illustration of the FLIm system is shown in Fig. 1. A frequency-tripled, 355 nm Nd:YAG Q-switched laser (SPOT-10–100-355; Elforlight, USA) was used for fluorescence excitation. The excitation beam was sampled (BSF10-UV beam splitter; Thorlabs, USA) to generate a low-jitter trigger signal for acquisition synchronization (DET10 photodetector; Thorlabs, USA). The excitation beam was delivered through a 4m length of multimode optical fiber (FG050UGA; Thorlabs, USA) to a custom-made handheld raster-scanning imaging probe, inside which the beam was collimated (lens L6), reflected (DM1, z337rdc dichroic mirror; Chroma Technology, USA), scanned (6200HM40 scanning system; Cambridge Technology, USA), and focused through a scanning relay system (L3 and L4, 30mm EFL; L5, 50mm EFL; Thorlabs, USA) onto the conjugated focal plane. Since a single laser pulse was needed per image pixel, the pixel acquisition rate was equal to the laser repetition rate (< 10 kHz).

The sample fluorescence emission was collected and collimated through the same scanning relay system (L3-L5), separated from the excitation beam (DM1), and transferred to a collection fiber (FG200UEA; Thorlabs, USA) connected to a multispectral module, which split the fluorescence emission into three spectral channels (S1-S3) by means of a set of dichroic mirrors (DM2: LM01–427-25; DM3: FF484-Fdi01; Semrock, USA) and optical filters (F1: FF01–390/40; F2: FF01–452/45; F3: FF01–496; Semrock, USA). Each of the three spectral channel outputs was transferred to an optical fiber (FG200UEA; Thorlabs,

USA) and the three fibers were coupled to a microchannel plate photomultiplier tube (MCP-PMT) (R3809U-50; Hamamatsu, Japan). These three optical fibers, with lengths of 1, 13, and 25 m, enabled time-multiplexing of the three spectral channels. The electrical output signal of the MCP-PMT was amplified (C5594–12; Hamamatsu, Japan) before being sampled at 2.5 GHz (PXIe-5160; National Instruments, USA). Laser trigger, scanning control, and acquisition operations were performed using a PC system with a user interface developed in LabVIEW (National Instruments, USA).

The handheld probe with a 140mm length rigid tube was designed to allow in vivo imaging of skin and to provide robust housing of the optical parts. The optical components were mounted on a custom machined aluminum plate and enclosed in a 3D-printed hard cover. The probe weighed less than 350 g and had 4m length cables and fibers, in order to allow access to the patient in a wide area from the mobile unit housing the FLIm system. The field of view (FOV) and lateral resolution were measured at 8.65 Å~ 8.65mm2 and 120 μm, respectively, by imaging the features of the 1951 USAF standard resolution target and calculating the line-spread function.

2.2. Clinical FLIm imaging of skin lesions

The FLIm dermoscope developed here was used to image skin lesionsfrom 38 patients recruited at the Skin Department of the Amaral Carvalho Cancer Hospital (Ja., S.o Paulo State, Brazil). The imaging study was approved by the Internal Review Board of the institution (CAAE: 71208817.5.00005434). Only patients presenting at least one lesion highly suspected as nBCC and scheduled for biopsy examination of that lesion were recruited. After signing a written informed consent form, each patient underwent the imaging protocol, immediately before the scheduled biopsy examination procedure. First, the suspected nBCC lesion was gently cleaned with a gauze soaked in a saline solution. Then, the tip of the FLIm imaging probe, previously disinfected using gauze soaked in 70 % ethanol, was placed in contact with the lesion and a multispectral FLIm was acquired. The imaging site was selected so that regions of both the lesion and the surrounding uninvolved (healthy) skin tissue were present within the FOV of the FLIm probe. Immediately after FLIm imaging, lesion tissue biopsy was performed, following standard procedures. Fig. 2A shows the handheld probe used to image the forearm region of a human subject.

All lesion FLIm images were acquired with an average laser excitation power of 10mW measured at the sample, a pixel rate of 10 kHz, and 140 × 140 pixels per image. These parameters corresponded to an acquisition time of 1.96 s and an excitation energy exposure of 1.52 mJ at the sample. For ethical approval, the safety of this equipment was evaluated by a specialized committee, considering current Brazilian legislation and scientific reports concerning similar systems used for in vivo applications [24–27]. The corresponding thermal and photochemical maximum permissible exposure (MPE) levels for skin were calculated, showing that the system used was in compliance with the guidelines of the American National Standards Institute (ANSI) for Safe Use of Lasers [28].

2.3. FLIm data analysis

The multispectral FLIm data is composed of fluorescence intensity temporal decay signals, $y_\lambda(x, y, t)$, measured at each emission spectral band (λ) and each spatial location or image pixel (x, y). First, multispectral absolute and normalized fluorescence intensity values were computed for each pixel as follows. The multispectral absolute fluorescence intensity $I_\lambda(x, y)$ was simply computed by numerically integrating the fluorescence intensity temporal decay signal: $I_\lambda(x, y) = \int y_\lambda(x, y, t)dt$

The multispectral normalized fluorescence intensity $I_{\lambda,n}(x, y)$ was computed from the multispectral absolute fluorescence intensities $I_\lambda(x,y)$ as follows:

$$I_{\lambda,n}(x, y) = \frac{I_\lambda(x, y)}{\sum_\lambda I_\lambda(x, y)}$$

In the context of time-domain FLIM data analysis, the fluorescence decay $y_\lambda(x, y, t)$ measured at each spatial location (x, y) can be modeled as the convolution of the fluorescence impulse response (FIR) $h_\lambda(x,y, t)$ of the sample and the measured instrument response function (IRF) $u_\lambda(t)$:

$$y_\lambda(x, y, t) = u_\lambda(t) * h_\lambda(x, y, t)$$

Therefore, to estimate the sample FIR $h_\lambda(x,y, t)$, the IRF $u_\lambda(t)$ needs to be temporally deconvolved from the measured fluorescence decay $y_\lambda(x, y, t)$. In this work, temporal deconvolution was performed using a nonlinear least squares iterative reconvolution algorithm, in which the FIR was modeled as a bi-exponential decay:

$$h_\lambda(x, y, t) = \alpha_{fast,\lambda}(x, y)e^{-t/\tau_{fast,\lambda}(x, y)} + \alpha_{slow,\lambda}(x, y)e^{-t/\tau_{slow,\lambda}(x, y)}$$

Here, $\tau_{fast,\lambda}(x, y)$ and $\tau_{slow,\lambda}(x, y)$ represent the time-constant (lifetime) of the fast and slow decay components, respectively; while $\alpha_{fast,\lambda}(x, y)$ and $\alpha_{slow,\lambda}(x, y)$ represent the relative contribution of the fast and slow decay components, respectively. Finally, the average fluorescence lifetime $\tau_{avg,\lambda}(x, y)$ for each pixel and emission spectral band were estimated from the FIR $h_\lambda(x, y, t)$ as follows:

$$\tau_{avg,\lambda} = \frac{\int t h_\lambda(x, y, z)dt}{\int h_\lambda(x, y, z)dt}$$

2.4. Statistical analysis

Regions of interest (ROI) in the images were manually selected, based on the clinical evaluation of the dermatologist. For each FLIm feature map of each lesion, one ROI was selected from an nBCC region and another ROI from a surrounding uninvolved region, and the median value for each ROI was calculated. Thus, each imaged lesion provided paired values of each FLIm parameter, corresponding to healthy and nBCC tissue regions from the

same patient. A paired t-test was applied to paired data of each FLIm feature to identify significant differences between the mean values of each FLIm parameter for healthy and nBCC tissues (sample size of 38). The significance level was set at 5% for all the paired t-tests, expecting medium and large effect sizes, where the test power could be higher than 0.9.

In order to quantify the potential of the FLIm features for discriminating nBCC from healthy tissue, a linear discriminant analysis was performed using three feature sets. The first used only the intensity parameters, while the second was built using only the lifetime parameters, and the third classifier was built using both intensity and lifetime parameters. The total set of 76 samples (38 from each class) was split into training and testing sets (75% and 25% of the total, respectively). To evaluate the classifiers, the receiver operator curve (ROC) area-under-the-curve (AUC) was calculated for the testing set. The optimal threshold was calculated based on the diagnostic odds ratio [29].

3. Results

3.1. Clinical FLIm imaging of nBCC skin lesions

A total of thirty-eight (38) skin lesions, confirmed to be nBCC by tissue biopsy histopathological evaluation, were successfully imaged using the multispectral FLIm dermoscope developed for this study (Fig. 2A). The clinical photograph of a sample skin lesion and its corresponding multispectral FLIm feature maps are shown in Fig. 2B and C. This sample lesion corresponded to an nBCC located on the left dorsal region of an 82-year-old female patient, measuring ~5×5 mm on the surface.

The lesion central region showed lower absolute intensities, relative to the surrounding uninvolved tissue (Fig. 2C (i-iii)). Although less contrast was observed between the lesion and the surrounding tissue in the relative intensity maps (Fig. 2C (iv-vi)), the lesion region showed increased spatial intensity variability (texture). Relative to the surrounding tissue, the lesion central region showed longer average and slow lifetimes in the>496 nm channel (Fig. 2C (ix, xii)), and shorter fast lifetimes in the 390 Å} 20 nm and 452 Å} 22 nm channels (Fig. 2C (xiii, xiv). Lower slow lifetime weight values were also observed for the lesion central region, compared to the surrounding uninvolved tissue (Fig. 2C (xvi-xviii)). Overall, these trends in the FLIm features observed for this particular lesion were consistent with the results from the statistical analysis performed for the mean ROI values, as summarized in the next section.

3.2. Exploratory statistical analysis of the FLIm features

A paired t-test was applied to the paired data for each FLIm feature (n=38), in order to assess the difference in the mean ROI values for the nBCC and healthy tissues (Fig. 3). The absolute intensity mean ROI values for nBCC were significantly lower across all the spectral channels ($p < 0.001$, Fig. 3(A–C)). For the normalized intensity, the mean ROI values for nBCC were significantly higher in channel 1 and lower in channel 2 ($p < 0.05$, Fig. 3(D and E)). The average lifetime mean ROI values for nBCC were significantly longer in channel 3 ($p < 0.001$, Fig. 3I). The slow lifetime mean ROI values for nBCC were significantly longer

in channel 1 ($p < 0.05$, Fig. 3J) and channel 3 ($p < 0.001$, Fig. 3L). In contrast, the fast lifetime mean ROI values for nBCC were significantly shorter across all channels ($p < 0.001$, Fig. 3(M–O)), and the same trend was observed for the slow lifetime weight ($p < 0.001$, Fig. 3(P–R)).

3.3. ROC curve analysis

Fig. 4 shows the test set ROC curves and the corresponding AUC values for the three classifiers. Features extracted only from lifetime parameters are represented by a solid line and circle markers, while intensity-only features are represented by a solid line and triangle markers. A gray dashed line with squares as markers represents the combined features, with both lifetime and intensity parameters together in the classifier. Although the intensity features proved to be good parameters, the classification could clearly be improved using both lifetime and intensity features. Furthermore, the lifetime parameters were shown to be the best features for this set. The lifetime features showed better performance, enabling higher sensitivity, together with high specificity. Table 1 summarizes the metrics for each classifier and feature set.

4. Discussion

Here, we report a multispectral FLIm dermoscope capable of fast (acquisition time<2 s), wide field (FOV~60 mm2), and label-free skin autofluorescence lifetime imaging using three spectral emission bands simultaneously. In vivo FLIm imaging of clinical skin lesions was performed for 38 patients presenting nBCC. FLIm dermoscopy imaging did not interfere with the clinical assessment, neither the tissue biopsy resection procedures scheduled for these patients. The large FOV enabled imaging not only of the entire visual extent of the lesions, but also the surrounding clinically normal tissue, which was a relevant feature for delineating lesion boundaries. The encouraging results obtained from this pilot study indicated the potential of FLIm dermoscopy for distinguishing between healthy and nBCC lesion tissues.

Demonstrations of endogenous FLIM imaging of skin have been reported previously. Multiphoton imaging was investigated using in vivo and ex vivo studies; although this technique can achieve high resolution and be used for deeper tissues, it typically has a limited FOV (usually 200 μm) and low speed of acquisition of lifetime images for clinical applications (tens of seconds) [30–33]. Single-photon lifetime imaging has also been reported in in vivo and ex vivo studies; although some of these studies have demonstrated great improvements in terms of FOV and speed, the techniques are benchtop-based and do not enable the use of multiple spectral channels. Furthermore, to the best of our knowledge, there have been no reports using this sample size of patients [15,17,24,26]. The multispectral FLIm dermoscope presented here, adapted from our previous design [24], overcomes some of the limitations of the previously reported imaging systems.

The multispectral FLIm dermoscope was designed to specifically measure tissue autofluorescence mainly originated from three endogenous fluorophores of interest. Skin tissue autofluorescence induced with an excitation wavelength of 355 nm and measured using the spectral emission band at 390 ± 20 nm is expected to originate predominantly from

collagen in the submucosa. Skin autofluorescence signals obtained using the spectral emission bands at 452 ± 22.5 nm and >496 nm are expected to originate predominantly from epithelial cell NADH and FAD, respectively. Therefore, this design enabled the use of multiple potential autofluorescence biomarkers of nBCC, as demonstrated by the results of the statistical analysis performed for each multispectral FLIm feature, which identified 11 that were statistically significantly different between healthy and nBCC tissues ($p < 0.001$; Fig. 3). Although further studies are needed to understand the observed differences in the FLIm features, the results suggested that these FLIm dermoscopic features could potentially represent novel autofluorescence biomarkers of nBCC.

The potential of using FLIM on the skin has been reported in previous studies. Using multiphoton imaging, in vivo photo-aging studies found lifetime differences between the upper and lower layers of the skin. However, no significant lifetime differences were found between young and elderly patients [30,32]. FLIM analyses of freshly excised lesions have been reported using both single and multiphoton imaging. Samples of nBCC and dysplasic nevus were compared using two spectral channels (380−500 nm and 500−640 nm), with excitation at 760 nm. Using both channels, significantly different lifetimes were observed, with a higher value for nBCC, compared to dysplasic nevus. For nBCC, lifetimes of 2.79 and 2.53 ns were obtained for each channel, respectively. These results showed the potential of the technique, despite a small FOV (< 1 mm.) [33].

The potential of single-photon FLIm for discriminating between healthy and BCC lesion tissues was first demonstrated using unfixed human tissue biopsy samples [15]. In that study, the distinction of BCC areas from the surrounding uninvolved skin tissue, based on autofluorescence lifetimes, was significantly more accurate than when autofluorescence intensities were used (ROC-AUC: ~0.9 for lifetimes vs. ~0.6 for intensities). Although the results were promising, the main limitations of the study were a small sample size (n=25) and the lack of in vivo FLIm data.

The results for intensity and lifetime FLIm obtained here (Fig. 3) corroborated the earlier findings. The absolute intensity, fast lifetime, and slow lifetime weight values were lower for the lesion region, compared to the surrounding tissue, while the average lifetime values showed less or no difference [15,17]. Similar results were found in an investigation of squamous cell carcinoma (SCC) in an animal model [19], where FLIm data were acquired by single-photon excitation at 480 nm and FAD fluorescence emission at 535 nm. The squamous cell carcinoma tissue presented lower values for short lifetimes and similar values for longer lifetimes, compared to healthy skin. The same trend was also found in an in vivo patient study, with excitation of BCC at 378 nm [16]. Although the present findings corroborated the ex vivo results mentioned above for the slow lifetime, the fast lifetime component for the 3rd spectral channel showed the opposite trend, with higher values for nBCC, compared to normal tissue. However, the same behavior of fast lifetime values for this spectral region was reported in an in vivo study of the autofluorescence lifetime of skin, using six patients [16].

It can be seen from Fig. 3 that some of the intensity and lifetime features presented overlapping between the distributions for the healthy and nBCC tissues. As expected, for

features whose distributions presented larger overlaps, there was no statistically significant difference. However, p-values lower than 0.001 were obtained for three steady-state and eight lifetime-associated features. As shown by the p-values, the lifetime features conveyed more information than the steady-state features, leading to higher classification scores, as shown in Table 1.

In this work, a small database of FLIm dermoscopy images from 38 in vivo human skin lesions, which were all confirmed as nBCC by biopsy histopathological evaluation, enabled exploration of the potential of this novel dermoscope to distinguish between healthy and nBCC lesion tissues. Using a combination of autofluorescence spectral and lifetime FLIm features within a linear discriminant analysis statistical classifier, regions of nBCC lesions could be discriminated from surrounding uninvolved tissue regions within the same dermoscope FOV, with encouraging estimated levels of sensitivity (88) and specificity (67). These very preliminary but encouraging results suggest that FLIm dermoscopy has the potential to provide in situ delineation of nBCC lesions. Given that surgical excision of malignant skin lesions is the most widely recommended treatment option, and that the rate of incomplete excision is closely dependent on the training and experience of the dermatologist, and can be as high as ~70 % [4,5,8], a dermatological imaging tool that can provide automated in situ delineations of malignant skin lesions could potentially result in significant increases of complete excision rates, consequently improving the clinical outcomes.

Although the reported multispectral FLIm dermoscope design enables safe clinical imaging of skin lesions, it still suffers from several limitations. Firstly, its acquisition speed is only suitable for snapshot imaging. In order to enable video-rate imaging, the pixel rate needs to be increased and the exposure excitation power needs to be decreased. The cost and physical dimensions of a dermoscopy system can also limit its adoption by dermatologists. Therefore, future efforts will focus on increasing acquisition speed and making FLIm dermoscopy systems both more cost-effective and portable. In addition, higher spatial resolution and a larger FOV would significantly enhance the functionality of this novel multispectral FLIm dermoscopy system.

The results of this pilot investigation suggest that FLIm dermoscopy has the potential to provide in situ delineation of nBCC lesions. However, this study is very preliminary and limited only to nBCC lesions. Future efforts will focus on acquiring a larger and more comprehensive database of FLIm dermoscopy images from in vivo human nonmalignant and malignant skin lesions. Such a database would enable quantification of the ability of this novel FLIm dermoscopy system to distinguish the most common and confounding benign skin lesions from the most common malignant skin lesions, as well as to delineate the true borders of the most common malignant skin lesions.

5. Conclusions

This paper describes a wide-field multispectral FLIm dermoscope and demonstrates its ability to safely image a range of autofluorescence features from in vivo clinical skin lesions of patients, at the physician’s office. To the best of our knowledge, this is the first

demonstration of multispectral autofluorescence lifetime wide-field imaging of in vivo human skin lesions. The ability of this novel FLIm dermoscope to seamlessly image skin tissue in clinical settings will facilitate the development and validation of new autofluorescence lifetime imaging capabilities that could potentially lead to improvements in the clinical management of skin cancer patients.

Acknowledgments

The authors would like to thank Professor Vanderlei S. Bagnato for scientific discussions. Financial support was provided by the following Brazilian funding agencies: Coordenacao de Aperfeicoamento de Pessoal de Nivel Superior - Brasil (CAPES - Finance Code 001); CNPq PVE (grants #401150/2014-3 and #314533/2014-1); and the Sao Paulo State Research Foundation (FAPESP, grants #2013/07276-1(CEPOF) and #2014/50857-8 (INCT)). Javier A. Jo was also supportedby the National Institute of Health (grant #R01CA218739).

References

1. Lomas A, Leonardi-Bee J, Bath-Hextall F, A systematic review of worldwide incidence of nonmelanoma skin cancer, Br. J. Dermatol 166 (2012) 1069–1080, 10.1111/j.1365-2133.2012.10830.x. [PubMed: 22251204]
2. Instituto nacional do c.ncer, Estimativa 2018: Incid.ncia De C.ncer No Brasil, (2017) https://doi.org/978-85-7318-283-5.
3. Ferlay J, Soerjomataram I, Dikshit R, Eser S, Mathers C, Rebelo M, Parkin DM, Forman D, Bray F, Cancer incidence and mortality worldwide: sources, methods and major patterns in GLOBOCAN 2012, Int. J. Cancer 136 (2015).
4. Holmkvist KA, Rogers GS, Dahl PR, Incidence of residual basal cell carcinoma in patients who appear tumor free after biopsy, J. Am. Acad. Dermatol 41 (1999) 600–605, 10.1016/S0190-9622(99)80061-9. [PubMed: 10495384]
5. Grelck K, Sukal S, Rosen L, Suciu GP, Incidence of residual nonmelanoma skin cancer in excisions after shave biopsy, Dermatologic Surg. 39 (2013) 374–380, 10.1111/dsu.12056.
6. Mogensen M, Jemec GBE, Diagnosis of nonmelanoma skin cancer/keratinocyte carcinoma: a review of diagnostic accuracy of nonmelanoma skin Cancer diagnostic tests and technologies, Dermatologic Surg. 33 (2007) 1158–1174, 10.1111/j.1524-4725.2007.33251.x.
7. Findlay M, Ally MS, Non-melanoma skin cancers, Plast. Reconstr. Surg John Wiley & Sons, Ltd, Chichester, UK, 2015, pp. 100–114, 10.1002/9781118655412.ch10.
8. Alaibac M, Facial basal cell carcinoma: analysis of recurrence and follow-up strategies, Oncol. Rep 26 (2011) 1423–1429, 10.3892/or.2011.1453. [PubMed: 21922143]
9. Siegel RL, Miller KD, Jemal A, Cancer statistics, 2018, CA Cancer J. Clin 68 (2018) 7–30, 10.3322/caac.21442. [PubMed: 29313949]
10. Heikal AA, Intracellular coenzymes as natural biomarkers for metabolic activities and mitochondrial anomalies, Biomark. Med 4 (2010) 241–263, 10.2217/bmm.10.1. [PubMed: 20406068]
11. Richards-Kortum R, Sevick-Muraca E, Quantitative optical spectroscopy for tissuediagnosis, Annu. Rev. Phys. Chem 47 (1996) 555–606, 10.1146/annurev.physchem.47.1.555. [PubMed: 8930102]
12. Croce AC, Bottiroli G, Autofluorescence spectroscopy and imaging: a tool for biomedical research and diagnosis, Eur. J. Histochem 58 (2014), 10.4081/ejh.2014.2461.
13. Panjehpour M, Julius CE, Phan MN, Vo-Dinh T, Overholt S, Laser-induced fluorescence spectroscopy for in vivo diagnosis of non-melanoma skin cancers, Lasers Surg. Med 31 (2002) 367–373, 10.1002/lsm.10125. [PubMed: 12430156]
14. Brancaleon L, Durkin AJ, Tu JH, Menaker G, Fallon JD, Kollias N, In vivo fluorescence spectroscopy of nonmelanoma skin cancer, Photochem. Photobiol 73 (2001) 178, 10.1562/0031-8655(2001)073<0178:IVFSON>2.0.CO;2. [PubMed: 11272732]

15. Galletly NP, McGinty J, Dunsby C, Teixeira F, Requejo-Isidro J, Munro I, Elson DS, Neil MAA, Chu AC, French PMW, Stamp GW, Fluorescence lifetime imaging distinguishes basal cell carcinoma from surrounding uninvolved skin, Br. J. Dermatol 159 (2008) 152–161, 10.1111/j.1365-2133.2008.08577.x. [PubMed: 18460029]
16. Saito Nogueira M, Cosci A, Teixeira Rosa RG, Salvio AG, Pratavieira S, Kurachi C, Portable fluorescence lifetime spectroscopy system for in-situ interrogation of biological tissues, J. Biomed. Opt 22 (2017) 1, 10.1117/1.JBO.22.12.121608.
17. De Beule PAA, Dunsby C, Galletly NP, Stamp GW, Chu AC, Anand U, Anand P, Benham CD, Naylor A, French PMW, A hyperspectral fluorescence lifetime probe for skin cancer diagnosis, Rev. Sci. Instrum 78 (2007) 123101, 10.1063/1.2818785. [PubMed: 18163714]
18. Na R, Stender I-M, Wulf HC, Can autofluorescence demarcate basal cell carcinoma from normal skin? A comparison with protoporphyrin IX fluorescence, Acta Derm. Venereol 81 (2001) 246–249, 10.1080/00015550152572859. [PubMed: 11720169]
19. Miller JP, Habimana-Griffin L, Edwards TS, Achilefu S, Multimodal fluorescence molecular imaging for in vivo characterization of skin cancer using endogenous and exogenous fluorophores, J. Biomed. Opt 22 (2017) 066007, 10.1117/1.JBO.22.6.066007.
20. McGinty J, Galletly NP, Dunsby C, Munro I, Elson DS, Requejo-Isidro J, Cohen P, Ahmad R, Forsyth A, Thillainayagam AV, Neil MAA, French PMW, Stamp GW, Wide-field fluorescence lifetime imaging of cancer, Biomed. Opt. Express 1 (2010) 627, 10.1364/BOE.1.000627. [PubMed: 21258496]
21. Chen B, Lu Y, Pan W, Xiong J, Yang Z, Yan W, Liu L, Qu J, Support vector machine classification of nonmelanoma skin lesions based on fluorescence lifetime imaging microscopy, Anal. Chem 91 (2019) 10640–10647, 10.1021/acs.analchem.9b01866. [PubMed: 31314502]
22. Cicchi R, Massi D, Sestini S, Carli P, De Giorgi V, Lotti T, Pavone FS, Multidimensional non-linear laser imaging of basal cell carcinoma, Opt. Express 15 (2007) 10135, 10.1364/OE.15.010135. [PubMed: 19547362]
23. Pires L, Nogueira MS, Pratavieira S, Moriyama LT, Kurachi C, Time-resolved fluorescence lifetime for cutaneous melanoma detection, Biomed. Opt. Express 5 (2014) 3080, 10.1364/BOE.5.003080. [PubMed: 25401022]
24. Cheng S, Cuenca RM, Liu B, Malik BH, Jabbour JM, Maitland KC, Wright J, Cheng Y-SL, Jo JA, Handheld multispectral fluorescence lifetime imaging system for in vivo applications, Biomed. Opt. Express 5 (2014) 921, 10.1364/BOE.5.000921. [PubMed: 24688824]
25. Malik BH, Lee J, Cheng S, Cuenca R, Jabbour JM, Cheng Y-SL, Wright JM, Ahmed B, Maitland KC, Jo JA, Objective detection of oral carcinoma with multispectral fluorescence lifetime imaging in vivo, Photochem. Photobiol 92 (2016) 694–701, 10.1111/php.12627. [PubMed: 27499123]
26. Cheng S, Rico-Jimenez JJ, Jabbour J, Malik B, Maitland KC, Wright J, Cheng Y-SL, Jo JA, Flexible endoscope for continuous in vivo multispectral fluorescence lifetime imaging, Opt. Lett 38 (2013) 1515–1517, 10.1364/OL.38.001515. [PubMed: 23632536]
27. Shrestha S, Applegate BE, Park J, Xiao X, Pande P, Jo JA, High-speed multispectral fluorescence lifetime imaging implementation for in vivo applications, Opt. Lett 35 (2010) 2558–2560, 10.1364/OL.35.002558. [PubMed: 20680057]
28. of America LI, American National Standard for Safe Use of Lasers, (2007) papers2://publication/uuid/D2E145A0-6015-4317-895E-3644589A4A40.
29. Glas AS, Lijmer JG, Prins MH, Bonsel GJ, Bossuyt PMM, The diagnostic odds ratio: a single indicator of test performance, J. Clin. Epidemiol 56 (2003) 1129–1135, 10.1016/S0895-4356(03)00177-X. [PubMed: 14615004]
30. Sanchez WY, Obispo C, Ryan E, Grice JE, Roberts MS, Changes in the redox state and endogenous fluorescence of in vivo human skin due to intrinsic and photoaging, measured by multiphoton tomography with fluorescence lifetime imaging, J. Biomed. Opt 18 (2012) 061217, 10.1117/1.JBO.18.6.061217.
31. Sanchez WY, Prow TW, Sanchez WH, Grice JE, Roberts MS, Analysis of the metabolic deterioration of ex vivo skin from ischemic necrosis through the imaging of intracellular NAD(P)H by multiphoton tomography and fluorescence lifetime imaging microscopy, J. Biomed. Opt 15 (2010) 046008, 10.1117/1.3466580.

32. Benati E, Bellini V, Borsari S, Dunsby C, Ferrari C, French P, Guanti M, Guardoli D, Koenig K, Pellacani G, Ponti G, Schianchi S, Talbot C, Seidenari S, Quantitative evaluation of healthy epidermis by means of multiphoton microscopy and fluorescence lifetime imaging microscopy, Skin Res. Technol 17 (2011) 295–303, 10.1111/j.1600-0846.2011.00496.x. [PubMed: 21518012]

33. Patalay R, Talbot C, Alexandrov Y, Munro I, Neil MAA, nig KK, French PMW, Chu A, Stamp GW, Dunsby C, Quantification of cellular autofluorescence of human skin using multiphoton tomography and fluorescence lifetime imaging in two spectral detection channels, Biomed. Opt. Express 2 (2011) 3295, 10.1364/boe.2.003295. [PubMed: 22162820]

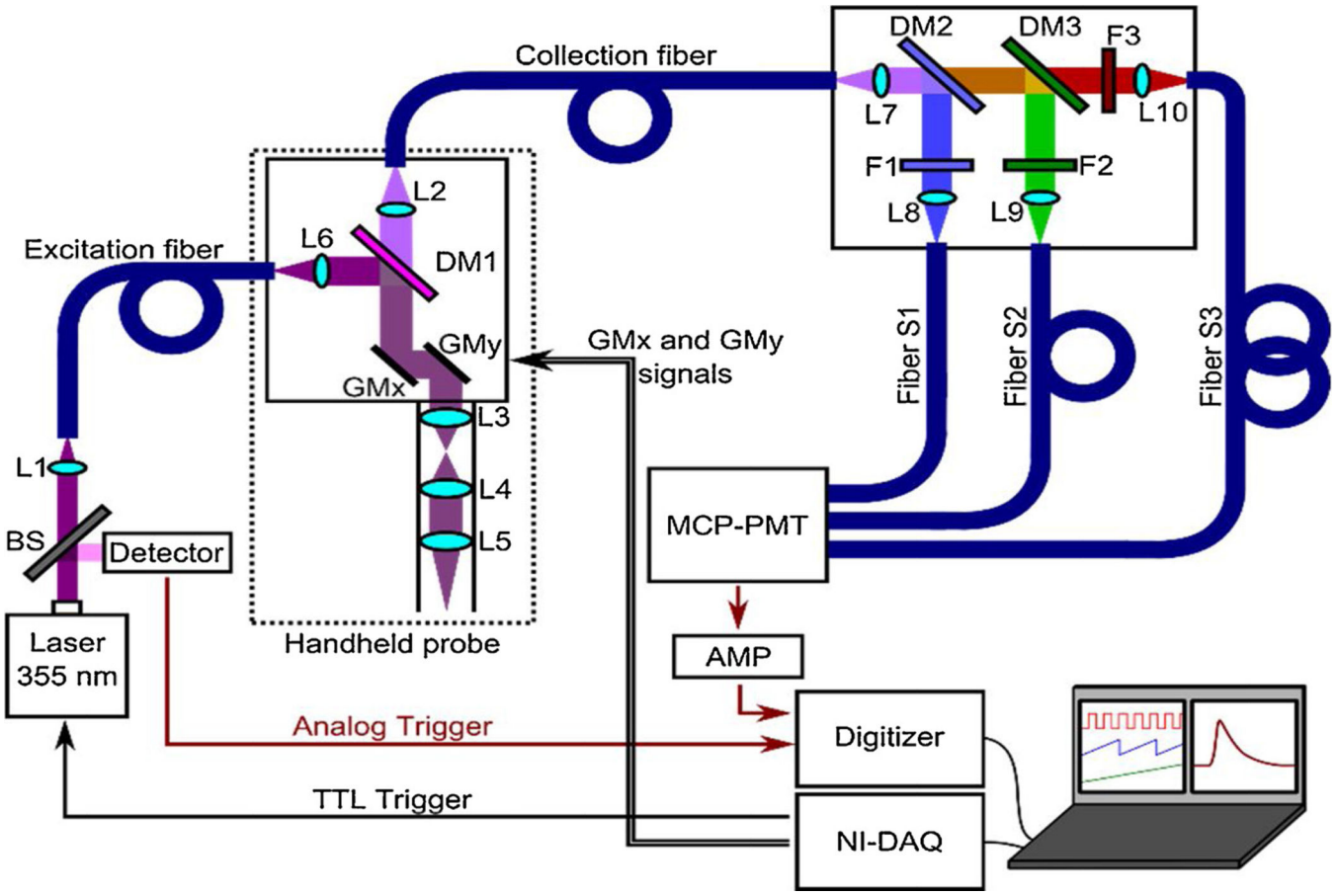

Fig. 1.

Multispectral FLIm dermoscopy system setup scheme. Light from the 355 nm laser is represented in violet color, while split fluorescence modules are represented in blue, green, and red. Fibers are represented in blue. The sample plane is located at the focus of lens L5.

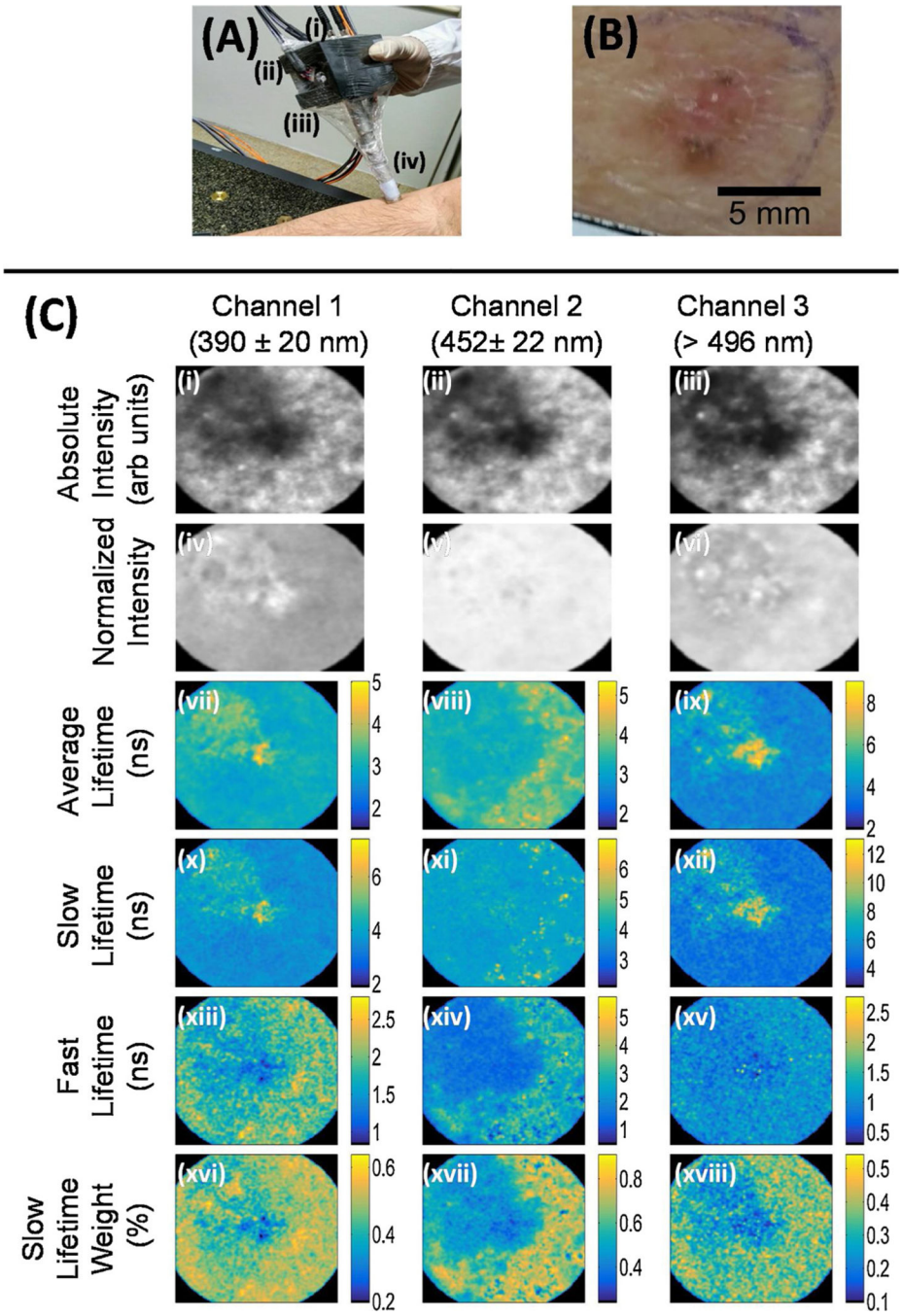

Fig. 2.

(A) Handheld FLIm dermoscope placed on the forearm region of a human subject. Excitation and acquisition fibers are attached at the back of the probe (i), while the galvo mirror controls are held laterally (ii) at the probe printed case (iii), above the rigid lens tube (iv). (B) Clinical photograph of the imaged nBCC lesion. (C) Multispectral FLIm parameter maps of the nBCC lesion. The columns show fluorescence parameters related to the three detection channels. Integrated intensity images are shown in the first row; the second row shows normalized intensity images; the third row shows the average lifetime image; further

rows show bi-exponential fitting parameters for the decay: slow and fast decays τ_{slow} and τ_{fast} in ns, and weight a_{fast}. The color maps indicate the values of the weights and decay times. The dimensions of the FLIm images are $8.65 \times 8.65\ mm^2$.

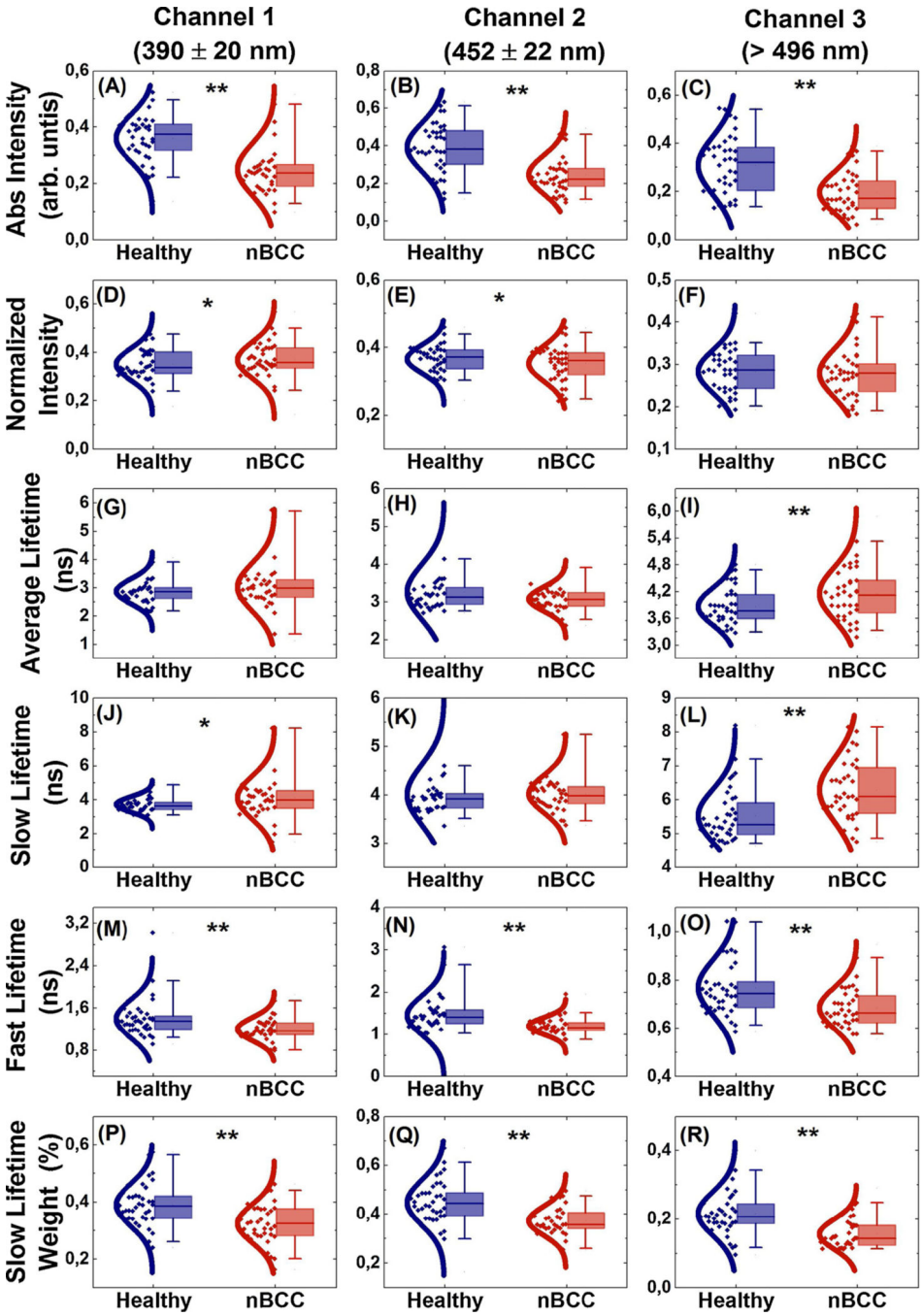

Fig. 3.

Boxplots of FLIm median values for healthy (blue) and nBCC (red) regions. From top to bottom, the rows show the integrated intensity (arb. units), normalized intensity, average, slow, and fast lifetime values (ns), and slow lifetime weight (%). The columns correspond to the three detection channels. Significant differences are indicated by * ($p < 0.05$) and ** ($p < 0.001$).

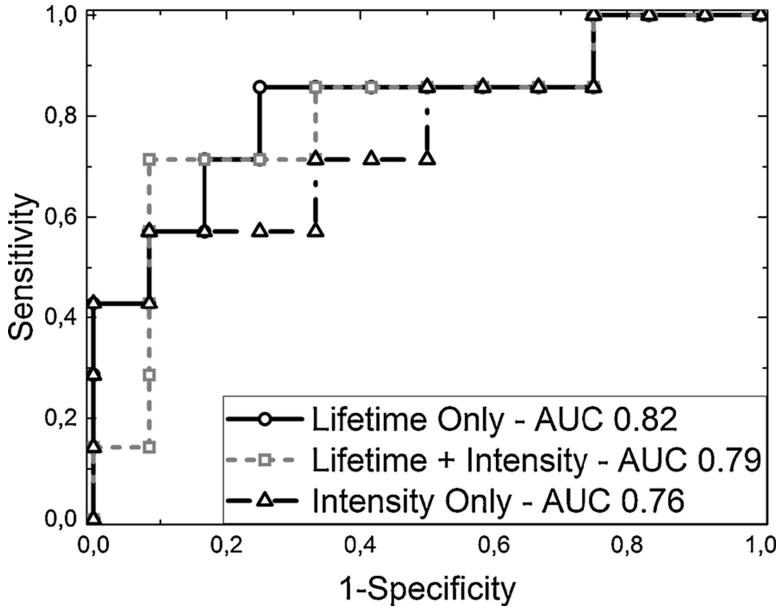

Fig. 4.

Classifier ROC curves and AUC values for the test set, using only intensity as input (dashed black line, triangle markers), both intensity and lifetime parameters (dotted gray line, square markers), and only lifetime parameters (solid black line, circle markers).

Table 1

Classification metrics for each feature set.

	Lifetime	Intensity	Combined
Sensitivity	0.86	0.57	0.88
Specificity	0.73	0.66	0.67
Accuracy	0.68	0.63	0.73
Precision	0.54	0.50	0.60
F-1 score	0.67	0.53	0.70